Available online at www.sciencedirect.com
SCIENCE DIRECT®
International Journal of Solids and Structures 43 (2006) 5674–5689
INTERNATIONAL JOURNAL OF SOLIDS and STRUCTURES
www.elsevier.com/locate/ijsolstr

Micromechanics-based constitutive modeling for unidirectional laminated composites

Z. Liang [a], H.K. Lee [b,*], W. Suaris [a]

[a] Department of Civil, Architectural and Environmental Engineering, University of Miami, Coral Gables, FL 33124-0620, United States
[b] Department of Civil and Environmental Engineering, Korea Advanced Institute of Science and Technology, Guseong-dong, Yuseong-gu, Daejon 305-701, Republic of Korea

Received 9 May 2005
Available online 10 January 2006

Abstract

A micromechanics-based constitutive model is developed to predict the effective mechanical behavior of unidirectional laminated composites. A newly developed Eshelby's tensor for an infinite circular cylindrical inclusion [Cheng, Z.Q., Batra, R.C., 1999. Exact Eshelby tensor for a dynamic circular cylindrical inclusion. J. Appl. Mech. 66, 563–565] is adopted to model the unidirectional fibers and is incorporated into the micromechanical framework. The progressive loss of strength resulting from the partial fiber debonding and the nucleation of microcracks is incorporated into the constitutive model. To validate the proposed model, the predicted effective stiffness of transversely isotropic composites under far field loading conditions is compared with analytical solutions. The constitutive model incorporating the damage models is then implemented into a finite element code to numerically characterize the elastic behavior of laminated composites. Finally, the present predictions on the stress–strain behavior of laminated composite plate containing an open hole is compared with experimental data to verify the predictive capability of the model.

Keywords: Unidirectional laminated composites; Micromechanics; Stiffness transformation; Damage modeling; Finite element implementation

1. Introduction

Fiber-reinforced laminated composites have been widely used as primary structural materials in fields of aerospace, transportation and other industrial applications due to their superior engineering properties (e.g., high stiffness and strength, low specific gravity and excellent flexibility). Recently, laminated composites have also been used to retrofit deteriorated infrastructures due to the superior qualities of these materials. The application to the rehabilitation and strengthening of the infrastructure includes bonding of laminated composite plates to reinforced concrete beams to improve flexural stiffness and strength, and wrapping of

* Corresponding author. Tel.: +82 42 869 3623.
E-mail address: leeh@kaist.ac.kr (H.K. Lee).

0020-7683/$ - see front matter © 2005 Published by Elsevier Ltd.
doi:10.1016/j.ijsolstr.2005.08.020

reinforced concrete columns with fiberglass/epoxy laminated jackets to provide flexural and shear strength enhancement to resist seismic loads and to increase axial capacity (Chajes and Januszka, 1995).

Laminated composites are composed of layered sheets of different materials that are bonded together. Lamination is used to combine the directional dependence of strength and stiffness of a material to obtain the best aspects of the constituent layers (Tungikar et al., 2004). Different from random chopped fiber-reinforced composites, the unidirectional fibers in laminated composites have different fiber orientations in different layers but have aligned distribution in the same layer. The fibers in laminated composites are generally considered to be continuous because of the large aspect ratio of fibers (ratio of fiber length to fiber diameter).

The key issue in the development of a constitutive model for laminated composites is how to incorporate the unidirectional continuous fibers into the constitutive relation. Although numerous constitutive models based on micromechanics have been proposed to model laminated composites, a micromechanical constitutive model incorporating infinite cylindrical inclusions, which required for modeling the unidirectional continuous fibers into the micromechanical framework, does not exist. In this study, a micromechanics-based constitutive model incorporating the infinite cylindrical inclusions is developed to accurately predict the overall elastic behavior of laminated composites.

In the present derivation, the unidirectional fibers are assumed to be circular cylindrical inclusions that are embedded in a matrix. A newly developed Eshelby's tensor for an infinite cylindrical inclusion (Cheng and Batra, 1999) is adopted to model the unidirectional fibers and is incorporated into the micromechanical framework. The progressive loss of strength resulting from the partial fiber debonding and the nucleation of microcracks is incorporated into the constitutive model. The Weibull's probabilistic function is used to model the varying probability of progressive fiber debonding and the nucleation of microcracks is simulated by adopting a continuum damage model proposed by Karihaloo and Fu (1989, 1990).

To validate the proposed constitutive model, the predicted effective stiffness of transversely isotropic composites under far field loading conditions is compared with analytical solutions (Herakovich, 1998). The constitutive model incorporating the damage models is then implemented into the finite element code ABAQUS (ABAQUS, 2002) to numerically characterize the elastic behavior of laminated composites. Finally, the implemented computational model is used to predict the effective elastic behavior of laminated composite plate containing an open hole and the prediction is compared with experimental data (Chang and Lessard, 1991) to verify the predictive capability of the model.

2. Micromechanics-based constitutive model for off-axis unidirectional fibrous composites

2.1. Overview

Let us consider an initially perfectly bonded, three-phase composite consisting of an elastic matrix (phase 0) with bulk modulus κ_0 and shear modulus μ_0, aligned continuous fibers (phase 1) with bulk modulus κ_1 and shear modulus μ_1, and (penny-shaped) microcracks (phase 2) of radius c. Since the aspect ratio of the fibers is nearly infinite as shown in Fig. 1, the fibers are assumed to be infinitely long, elastic cylindrical inclusions. Penny-shaped microcracks are regarded as the limiting case of aligned spheroidal voids with the aspect ratio $\alpha_2 \to 0$.

When inclusions (phases 1 and 2) are aligned, the composite as a whole is transversely isotropic. As loadings or deformations proceed, some fibers in the composite are partially debonded (phase 3) and microcracks are nucleated. Following Zhao and Weng (1996, 1997), a partially debonded fiber is replaced by an equivalent, perfectly bonded fiber that possesses transversely isotropic moduli. The nucleation of microcracks is simulated by adopting a continuum damage model proposed by Karihaloo and Fu (1989).

The local stresses, strains and stiffnesses at a typical point within a representative volume element (RVE) of the composite can be obtained by averaging over the ensemble of all statistical realizations of the fibers and microcracks. Eshelby's tensor for a spheroidal inclusion was previously derived by Sun (1998) and is employed here to model penny-shaped microcracks. The details of the implementation of the Eshelby's tensor for a spheroidal inclusion into the micromechanical framework can be found in Lee and Simunovic (2001). Eshelby's tensor for an infinite cylindrical inclusion to model the unidirectional fibers and the constitutive relation of laminated composites are explained in detail in the next section.

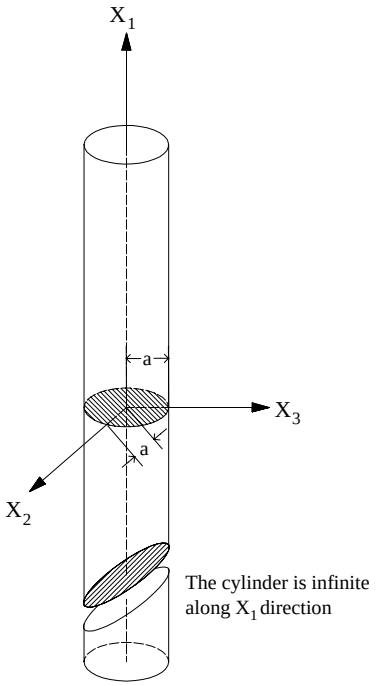

Fig. 1. Schematic description of a circular cylindrical inclusion.

2.2. Recapitulation of Eshelby's tensor for an infinite cylindrical inclusion

The aspect ratio of the unidirectional fibers in laminated composites is nearly infinity; thus, the Eshelby's tensor for a spheroidal inclusion is no longer appropriate to model the unidirectional fibers. Instead, a newly developed Eshelby's tensor for an infinite cylindrical inclusion by Cheng and Batra (1999) is adopted to model the unidirectional fibers and is incorporated into the micromechanical framework. The summary of the Eshelby's tensor for an infinite cylindrical inclusion is repeated here for completeness of the proposed constitutive model.

Closed-form, time-harmonic elastic field equations caused by an infinitely long, cylindrical inclusion in an elastic matrix were investigated by Cheng and Batra (1999) to derive the Eshelby's tensor for the inclusion. According to Eshelby (1957, 1961) and Mura (1982), the time-harmonic eigenstrain for an inclusion embedded in an infinite linear elastic medium (i.e., R^3) is defined as

$$\boldsymbol{\epsilon}^*(\mathbf{x},t) = \Lambda(\Omega)\mathrm{e}^{-\mathrm{i}\omega t}\boldsymbol{\epsilon}^{\Omega}(\mathbf{x}), \tag{1}$$

with

$$\Lambda(\Omega) = \begin{cases} 1, & \mathbf{x} \in \Omega; \\ 0, & \mathbf{x} \in R^3 - \Omega; \end{cases} \tag{2}$$

where Ω denotes the region occupied by the inclusion and ω signifies an angular frequency (Cheng and Batra, 1999). Fig. 1 shows the schematic description of a circular cylindrical inclusion in which $x_2^2 + x_3^2 < a^2$ and $-\infty < x_1 < \infty$. Following Mikata and Nemat-Nasser (1990, 1991), the perturbance strain fields induced by distributed eigenstrain $\boldsymbol{\epsilon}^*$ can be expressed as

$$\tilde{\boldsymbol{\epsilon}}(\mathbf{x}) = \int_V \mathbf{G}(\mathbf{x}-\mathbf{x}') : \boldsymbol{\epsilon}^*(\mathbf{x}')\,\mathrm{d}\mathbf{x}', \tag{3}$$

where ":" denotes the tensor contraction, $\mathbf{x}$ is the local point in the medium and $\mathbf{x}'$ resides in the inclusion. In addition, $\mathbf{G}$ is the second derivative of Green's function in a linear elastic medium. If we neglect the inter-inclusion interaction effects, then the perturbance strain fields in Eq. (3) can be rewritten as

$$\tilde{\boldsymbol{\epsilon}} = \mathbf{M} : \boldsymbol{\epsilon}^*, \tag{4}$$

with

$$\mathbf{M} = \int_V \mathbf{G}(\mathbf{x} - \mathbf{x}')\,\mathrm{d}\mathbf{x}', \tag{5}$$

where $\mathbf{M}$ denotes the dynamic Eshelby's tensor for an infinite circular cylindrical inclusion and was explicitly derived by Cheng and Batra (1999):

$$M_{ijkl}(\mathbf{x}) = \tfrac{1}{2}\big[J_{ikl,j}(\mathbf{x}) + J_{jkl,i}(\mathbf{x})\big], \tag{6}$$

where

$$J_{ikl}(\mathbf{x}) = \frac{1}{4\pi\rho_1\omega^2}\left\{\lambda_1\delta_{kl}f_{,imm}(\mathbf{x},\alpha) + 2\mu_1[f_{,ikl}(\mathbf{x},\alpha) - f_{,ikl}(\mathbf{x},\beta)] - \mu_1\beta^2[\delta_{ik}f_{,l}(\mathbf{x},\beta) + \delta_{il}f_{,k}(\mathbf{x},\beta)]\right\}, \tag{7}$$

with

$$f(\mathbf{x},k) = \int_\Omega \frac{\mathrm{e}^{\mathrm{i}kr}}{r}\,\mathrm{d}\mathbf{x}', \tag{8}$$

$$r^2 = (x_k - x_k')(x_k - x_k'), \qquad \alpha^2 = \frac{\rho_1\omega^2}{\lambda_1 + 2\mu_1}, \qquad \beta^2 = \frac{\rho_1\omega^2}{\mu_1}. \tag{9}$$

Here, λ_1 and μ_1 are the Lame constants of the fibers, ρ_1 is the mass density of the fibers and δ_{ij} is the Kronecker delta.

The (interior) Eshelby's tensor $S_{ijkl}(\mathbf{x})$ for quasi-static deformations can be obtained from the dynamic Eshelby's tensor $\mathbf{M}$ in Eq. (6) by letting $\omega \to 0$

$$S_{ijkl}(\mathbf{x}) = \lim_{\omega\to 0}[M_{ijkl}(\mathbf{x})] = \tfrac{1}{2}\Big[J^S_{ikl,j}(\mathbf{x}) + J^S_{jkl,i}(\mathbf{x})\Big], \tag{10}$$

where $J^S_{ikl}(\mathbf{x})$ are given in Eqs. (24) and (25) of Cheng and Batra (1999). Since $S_{ijkl} = S_{jikl} = S_{ijlk}$, the non-zero components of the Eshelby's tensor for the inside of the infinite circular cylindrical inclusion can be expressed as (Cheng and Batra, 1999)

$$S_{ijkl} = \frac{4\nu_1 - 1}{8(1-\nu_1)}\delta_{ij}\delta_{kl} + \frac{3 - 4\nu_1}{8(1-\nu_1)}(\delta_{ik}\delta_{jl} + \delta_{il}\delta_{jk}), \tag{11}$$

$$S_{3j3l} = \frac{1}{4}\delta_{jl}, \tag{12}$$

$$S_{ij33} = \frac{\nu_1}{2(1-\nu_1)}\delta_{ij}, \tag{13}$$

where ν_1 denotes the Poisson's ratio of the fibers.

The fourth-rank Eshelby's tensor $S_{ijkl}(\mathbf{x})$ in Eqs. (11)–(13) can be rephrased as

$$S_{ijkl}(\mathbf{x}) = \widetilde{F}_{ijkl}(s_1, s_2, s_3, s_4, s_5, s_6), \tag{14}$$

where a transversely isotropic fourth-rank tensor $\widetilde{\mathbf{F}}$ is defined by six parameters b_m $(m = 1, \ldots, 6)$:

$$\begin{aligned}\widetilde{F}_{ijkl}(b_m) = {} & b_1\tilde{n}_i\tilde{n}_j\tilde{n}_k\tilde{n}_l + b_2(\delta_{ik}\tilde{n}_j\tilde{n}_l + \delta_{il}\tilde{n}_j\tilde{n}_k + \delta_{jk}\tilde{n}_i\tilde{n}_l + \delta_{jl}\tilde{n}_i\tilde{n}_k) + b_3\delta_{ij}\tilde{n}_k\tilde{n}_l + b_4\delta_{kl}\tilde{n}_i\tilde{n}_j + b_5\delta_{ij}\delta_{kl} \\ & + b_6(\delta_{ik}\delta_{jl} + \delta_{il}\delta_{jk}),\end{aligned} \tag{15}$$

with the unit direction vector $\tilde{\mathbf{n}}$ and index $m = 1, \ldots, 6$. If the 1-direction is chosen to be symmetric, then we have $\tilde{n}_1 = 1$, $\tilde{n}_2 = \tilde{n}_3 = 0$. Additionally, the six parameters on the right-hand side of Eq. (14) take the form:

$$s_1 = \frac{4 - 8\nu_1}{8(1 - \nu_1)}, \tag{16}$$

$$s_2 = \frac{2\nu_1 - 1}{8(1 - \nu_1)}, \tag{17}$$

$$s_3 = \frac{1}{8(1 - \nu_1)}, \tag{18}$$

$$s_4 = \frac{1}{8(1 - \nu_1)}, \tag{19}$$

$$s_5 = \frac{4\nu_1 - 1}{8(1 - \nu_1)}, \tag{20}$$

$$s_6 = \frac{2 - 3\nu_1}{8(1 - \nu_1)}. \tag{21}$$

The details of the derivation of the Eshelby's tensor for an infinite cylindrical inclusion can be found in Cheng and Batra (1999).

2.3. Stress–strain relation for unidirectional fibrous composites

As explained in Section 2.1, some fibers in the composite are partially debonded and microcracks are nucleated as deformations proceed. The overall composite system is regarded as a transversely isotropic material. By designating the 1-direction as axisymmetric axis and the plane 2–3 to be the transversely isotropic plane, the stress–strain relation of a typical transversely isotropic solid can be written as (see also Ju and Lee, 2001)

$$\begin{pmatrix} \sigma_{11} \\ \sigma_{22} \\ \sigma_{33} \\ \sigma_{23} \\ \sigma_{13} \\ \sigma_{12} \end{pmatrix} = \begin{bmatrix} C_{11} & C_{12} & C_{12} & 0 & 0 & 0 \\ C_{12} & C_{22} & C_{23} & 0 & 0 & 0 \\ C_{12} & C_{23} & C_{22} & 0 & 0 & 0 \\ 0 & 0 & 0 & C_{44} & 0 & 0 \\ 0 & 0 & 0 & 0 & C_{55} & 0 \\ 0 & 0 & 0 & 0 & 0 & C_{55} \end{bmatrix} \begin{pmatrix} \epsilon_{11} \\ \epsilon_{22} \\ \epsilon_{33} \\ 2\epsilon_{23} \\ 2\epsilon_{13} \\ 2\epsilon_{12} \end{pmatrix}. \tag{22}$$

In accordance with the notation given by Hill (1964), the components of the stiffness matrix can be rewritten as

$$\begin{aligned} &\frac{C_{22} + C_{23}}{2} = k, \qquad C_{12} = l, \qquad C_{11} = n, \\ &\frac{C_{22} - C_{23}}{2} = C_{44} = m, \qquad C_{55} = p, \end{aligned} \tag{23}$$

where k is the plane stress bulk modulus for the lateral dilatation without longitudinal extension ($k = \kappa + \frac{\mu}{3}$); m is the rigidity modulus for shearing in any transverse direction; n denotes the modulus for the longitudinal uniaxial straining; l denotes the associated cross-modulus; and p signifies the axial shear modulus (Hill, 1964).

Based on the governing field equations for linear elastic composites containing arbitrarily non-aligned and/or dissimilar inclusions (Ju and Chen, 1994), the effective stiffness tensor $\mathbf{C}_*$ for the four-phase composite can be derived as

$$\mathbf{C}_* = \mathbf{C}_0 \cdot \left[\mathbf{I} + \sum_{r=1}^{3} \left\{ \phi_r (\mathbf{A}_r + \mathbf{S}_r)^{-1} \cdot \left[\mathbf{I} - \phi_r \mathbf{S}_r \cdot (\mathbf{A}_r + \mathbf{S}_r)^{-1} \right]^{-1} \right\} \right], \tag{24}$$

in which "·" denotes the tensor multiplication, $\mathbf{C}_r$ is the elasticity tensor of the rth phase, $\mathbf{I}$ is the fourth-rank identity tensor, and ϕ_r signifies the volume fraction of the rth phase inclusion. The Eshelby's tensors $\mathbf{S}_1$ and $\mathbf{S}_3$ for perfectly bonded and partially debonded unidirectional fibers, respectively, are given in Eq. (14) and the

Eshelby's tensor $\mathbf{S}_2$ for penny-shaped microcracks was previously derived by Sun (1998). In addition, the fourth-rank tensor $\mathbf{A}_r$ is defined as

$$\mathbf{A}_r \equiv (\mathbf{C}_r - \mathbf{C}_0)^{-1} \cdot \mathbf{C}_0. \tag{25}$$

Accordingly, the effective elastic stiffness tensor $\mathbf{C}_*$ for the four-phase composites can be derived as

$$\mathbf{C}_* = \widetilde{F}_{ijkl}(\tau_1, \tau_2, \tau_3, \tau_4, \tau_5, \tau_6), \tag{26}$$

where the six parameters in Eq. (26) are given in Appendix A and have the following relation:

$$\tau_1 = k + n + m - 4p - 2l, \tag{27}$$
$$\tau_2 = -m + p, \tag{28}$$
$$\tau_3 = -k + m + l, \tag{29}$$
$$\tau_4 = -k + m + l, \tag{30}$$
$$\tau_5 = k - m, \tag{31}$$
$$\tau_6 = m. \tag{32}$$

Thus, the components of the stiffness matrix can be derived as

$$C_{11} = n = \tau_1 + 4\tau_2 + \tau_3 + \tau_4 + \tau_5 + 2\tau_6, \tag{33}$$
$$C_{12} = C_{13} = l = \tau_4 + \tau_5, \tag{34}$$
$$C_{22} = k + m = \tau_5 + 2\tau_6, \tag{35}$$
$$C_{23} = k - m = \tau_5, \tag{36}$$
$$C_{44} = m = \tau_6, \tag{37}$$
$$C_{55} = p = \tau_2 + \tau_6. \tag{38}$$

2.4. Stiffness transformation for off-axis unidirectional fibrous composites

In Section 2.3, the 1-direction is chosen to be fiber direction and the plane 2–3 corresponds to the transversely isotropic plane in unidirectional fibrous composites as shown in Fig. 2. Now we consider rotations through an angle θ about the X_3-axis to derive the stiffness of off-axis unidirectional fibrous composites. The angle θ is measured positive counterclockwise from the X_1-axis to the x_1-axis as shown in Fig. 3.

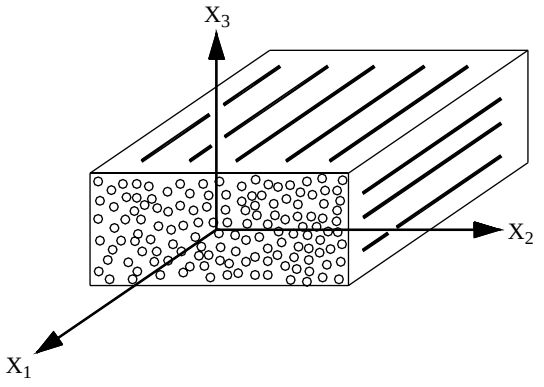

Fig. 2. Coordinates for a transversely isotropic material (see also Fig. 3.6 of Herakovich, 1998).

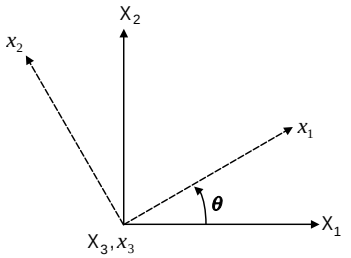

Fig. 3. Transformation about an axis.

Following the stiffness transformation law by Herakovich (1998), we have the following stress and strain transformations:

$$\boldsymbol{\sigma}_\alpha = \mathbf{C} : \boldsymbol{\epsilon}_\alpha = \mathbf{T}_1 : \boldsymbol{\sigma}_\beta, \tag{39}$$

$$\boldsymbol{\epsilon}_\alpha = \mathbf{T}_2 : \boldsymbol{\epsilon}_\beta, \tag{40}$$

where the stiffness matrix of the unidirectional fibrous composites $\mathbf{C}$ is given in Eq. (22); the subscript α signifies stress and strain matrices in the principal coordinate system ($x_1x_2x_3$); the subscript β denotes stress and strain matrices in the global coordinate system ($X_1X_2X_3$); and the transformation matrices $\mathbf{T}_1$ and $\mathbf{T}_2$ are rendered in Appendix B (see also Herakovich, 1998).

By combining Eqs. (39) and (40), the stiffness matrix of off-axis unidirectional fibrous composites $\overline{\mathbf{C}}$, which is the transformed stiffness matrix through an arbitrary angle θ about the X_3-axis, is derived as

$$\boldsymbol{\sigma}_\beta = \mathbf{T}_1^{-1} \cdot \mathbf{C} \cdot \mathbf{T}_2 : \boldsymbol{\epsilon}_\beta \equiv \overline{\mathbf{C}} : \boldsymbol{\epsilon}_\beta, \tag{41}$$

where the stiffness matrix of the unidirectional fibrous composites with the fibers oriented off-axis takes the form:

$$\overline{\mathbf{C}} = \begin{bmatrix} \overline{C}_{11} & \overline{C}_{12} & \overline{C}_{13} & 0 & 0 & \overline{C}_{16} \\ \overline{C}_{12} & \overline{C}_{22} & \overline{C}_{23} & 0 & 0 & \overline{C}_{26} \\ \overline{C}_{13} & \overline{C}_{23} & \overline{C}_{33} & 0 & 0 & \overline{C}_{36} \\ 0 & 0 & 0 & \overline{C}_{44} & \overline{C}_{45} & 0 \\ 0 & 0 & 0 & \overline{C}_{45} & \overline{C}_{55} & 0 \\ \overline{C}_{16} & \overline{C}_{26} & \overline{C}_{36} & 0 & 0 & \overline{C}_{66} \end{bmatrix}. \tag{42}$$

Here, the components of $\overline{\mathbf{C}}$ are given in Appendix C. It should be noted that the overall properties of off-axis unidirectional fibrous composites should be modeled as an anisotropic material. The details of the stiffness transformation for the off-axis unidirectional laminated composites can be found in Herakovich (1998).

3. Damage models

Following Zhao and Weng (1996, 1997) and Ju and Lee (2000), the probability of partial debonding of the unidirectional fibers is modeled as a two-parameter Weibull process. The cumulative probability distribution function of fiber debonding (damage) P_d at the level of hydrostatic tensile stress $(\bar{\boldsymbol{\sigma}}_m)_1$ can be expressed as

$$P_d[(\bar{\boldsymbol{\sigma}}_m)_1] = 1 - \exp\left[-\left(\frac{(\bar{\boldsymbol{\sigma}}_m)_1}{S_o}\right)^M\right] \tag{43}$$

with $(\bar{\boldsymbol{\sigma}}_m)_1 = \left(1 - \frac{2}{3}\nu_1\right)(\bar{\sigma}_{kk})_1$, where $(\bar{\sigma}_{kk})_1$ is the average hydrostatic tensile stress of the fibers. In addition, the constants S_o and M are the Weibull parameters. Therefore, the current partially debonded (damaged) fiber volume fraction ϕ_3 at a given level of $(\bar{\boldsymbol{\sigma}}_m)_1$ is given by

$$\phi_3 = \phi P_d[(\bar{\boldsymbol{\sigma}}_m)_1] = \phi\left\{1 - \exp\left[-\left(\frac{(\bar{\boldsymbol{\sigma}}_m)_1}{S_o}\right)^M\right]\right\}, \tag{44}$$

where ϕ is the original fiber volume fraction. The formulation for the internal stresses of fibers needed to initiate interfacial debonding can be found in Lee and Simunovic (2001) and Lee and Liang (2004).

According to a damage model for the nucleation of flaws in concrete like materials (Karihaloo and Fu, 1989, 1990), the density of nucleated microcracks in the composite can be defined as the following isotropic scalar function

$$\phi_2 = \begin{cases} \phi_{v0}, & \epsilon^a \leqslant \epsilon^{th}; \\ \phi_{v0} + c_1\left(1 - \dfrac{\epsilon^{th}}{\epsilon^a}\right)^{c_2}, & \epsilon^a > \epsilon^{th}; \end{cases} \tag{45}$$

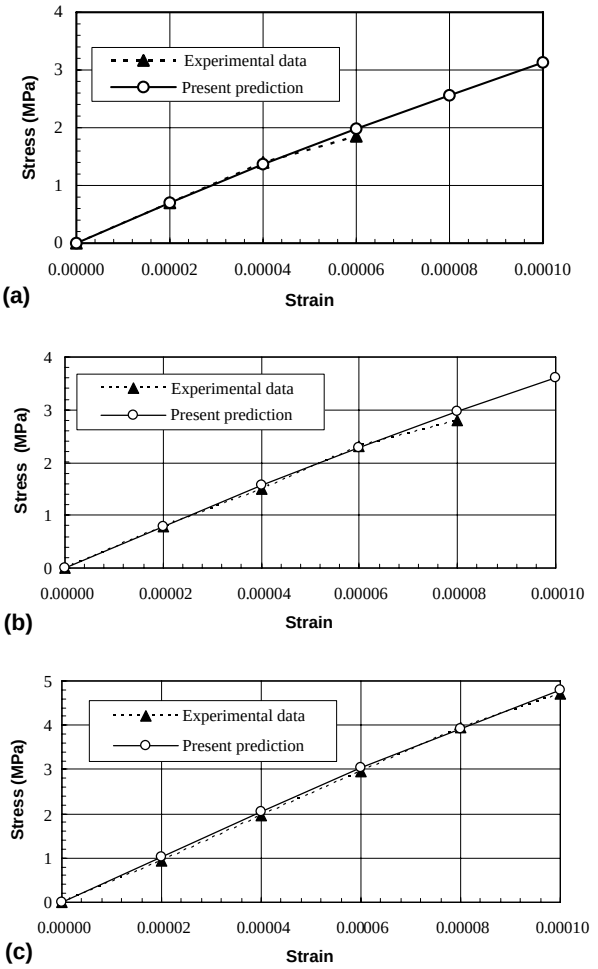

Fig. 4. Comparison of stress–strain curves of plain concrete between the present predictions and experimental data (Karihaloo and Fu, 1989). (a) Concrete mix A: $E_0 = 28.97$ GPa, $\nu_0 = 0.175$; (b) Concrete mix B: $E_0 = 32.24$ GPa, $\nu_0 = 0.180$; (c) Concrete mix C: $E_0 = 39.08$ GPa, $\nu_0 = 0.210$.

where ϕ_{v0} is the initial density of microcracks. $\epsilon^{\text{th}} = \sqrt{\epsilon^{\text{th}}_{ij}\epsilon^{\text{th}}_{ij}}$ is the effective strain threshold below which no nucleation takes place, c_1 and c_2 are material constants that depend on the specific shape and distribution of microcracks, and $\epsilon^{\text{a}} = \sqrt{\epsilon_{ij}\epsilon_{ij}} = \left[\epsilon_{11}^2 + \epsilon_{22}^2 + \epsilon_{33}^2 + 2(\epsilon_{12}^2 + \epsilon_{23}^2 + \epsilon_{31}^2)\right]^{1/2}$ is the current accumulated effective strain (Karihaloo and Fu, 1989).

To illustrate the damage constitutive behavior of the present framework, we predict the uniaxial stress–strain behavior of plain concrete using the present constitutive model incorporating the damage models and the prediction is compared with experimental data reported by Karihaloo and Fu (1989). Here, we adopt the material properties for three concrete mixes according to Karihaloo and Fu (1989) as follows: (i) Concrete mix A: $E_0 = 28.97$ GPa, $v_0 = 0.175$; (ii) Concrete mix B: $E_0 = 32.24$ GPa, $v_0 = 0.18$; (iii) Concrete mix C: $E_0 = 39.08$ GPa, $v_0 = 0.21$. The predicted stress–strain curves for the three concrete mixes against the experimental data (Karihaloo and Fu, 1989) are depicted in Fig. 4. It is observed from the figure that the present predictions match very well with the experimental data.

4. Numerical simulations and experimental comparison

4.1. Prediction of the effective stiffness of transversely isotropic composites under far-field loading conditions

The proposed constitutive model is exercised numerically to derive the effective stiffness of transversely isotropic composites. The predictions are compared with analytical solutions (Herakovich, 1998) to show the validity of the predictive capability of the model. Herakovich (1998) derived constitutive equations describing the elastic response of T300/5208 carbon/epoxy composite. The composite is transversely isotropic with a transformation angle θ varying from 0° to 90°. In this simulation, we employ the same material properties for the T300/5208 carbon/epoxy composites as those in Herakovich (1998) as follows: $E_0 = 4.62$ GPa, $v_0 = 0.36$, $\phi_0 = 0.62$; $E_1 = 227.53$ GPa, $v_1 = 0.20$, $\phi_1 = 0.001$. We compute the effective stiffness of the composites under far-field loading conditions.

The comparison of diagonal stiffness components C_{11}, C_{44}, C_{66} and off-diagonal stiffness components C_{16}, C_{26}, C_{36} of T300/5208 carbon/epoxy composites between the present predictions and analytical solutions (Herakovich, 1998) are shown in Figs. 5 and 6, respectively. It is noted from the figures that the responses obtained by the present prediction are slightly higher than those based on the analytical solutions since the

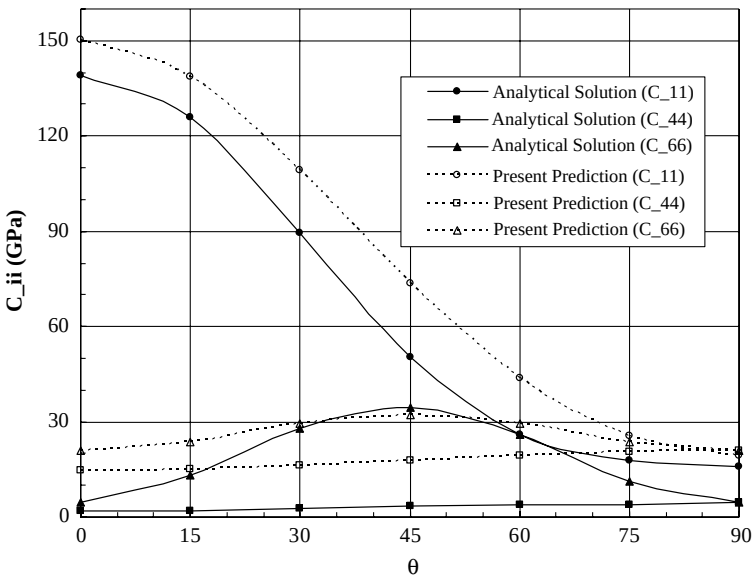

Fig. 5. Comparison of diagonal stiffness components C_{11}, C_{44}, C_{66} of T300/5208 carbon/epoxy composites between the present predictions and analytical solutions (Herakovich, 1998).

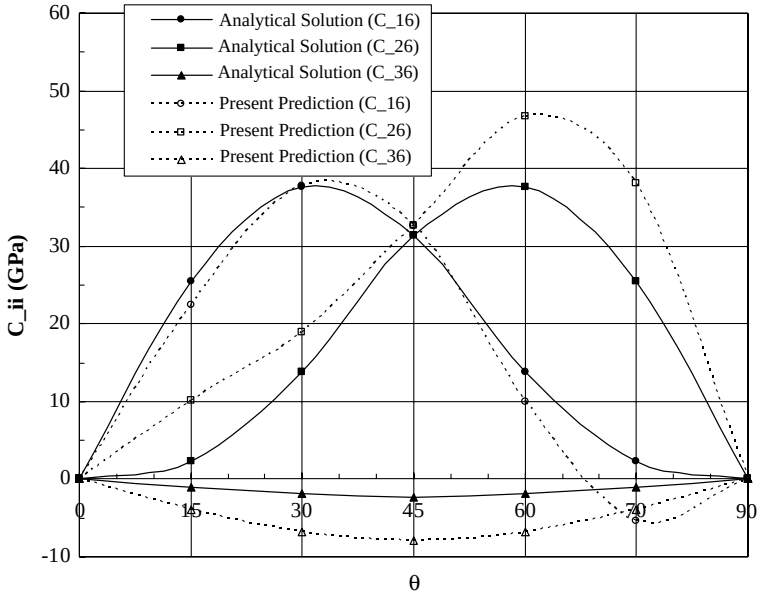

Fig. 6. Comparison of off-diagonal stiffness components C_{16}, C_{26}, C_{36} of T300/5208 carbon/epoxy composites between the present predictions and analytical solutions (Herakovich, 1998).

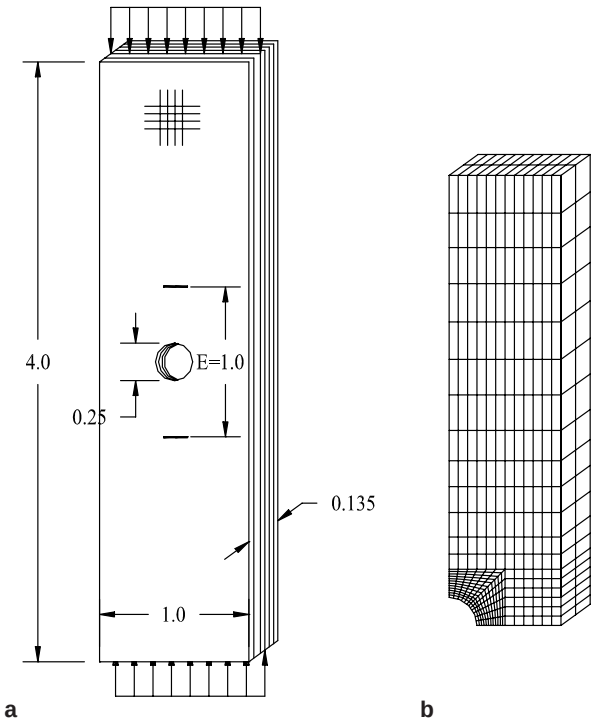

Fig. 7. Geometrical and finite element models for the laminated plate used in the simulation (see also ABAQUS, 2002).

present framework based on far-field loading conditions does not account for the boundary conditions of the composite specimens.

4.2. Experimental comparison of the response and damage behavior of a laminated composite plate with an open hole

The constitutive model is implemented into the finite element (FE) code ABAQUS installed on the IBM supercomputer using a user-supplied material subroutine to solve boundary-value problems. The details of implementation of a constitutive model into the FE code can be found in Lee and Shin (2004) and Lee and Liang (2004). To verify the implemented computational model, we compare the predicted stress–strain response of a laminated composite plate with an open hole with the experimental data provided by Chang and Lessard (1991). The plate is made of T300/976 graphite-epoxy resin prepreg tapes and is loaded in compression in the length direction. The ply orientations of the plate are cross-ply: $[(0/90)_6]_s$. The details of the specimen configuration is illustrated in Fig. 7(a).

Three-dimensional, constant-strain elements available in ABAQUS are used to model the plate where fine meshes are used in the vicinity of the hole as shown in Fig. 7(b). Similar to the ABAQUS sample simulation (ABAQUS, 2002), all plies in the plate are assumed to be 0° and 90° directions for simplicity. The thickness of

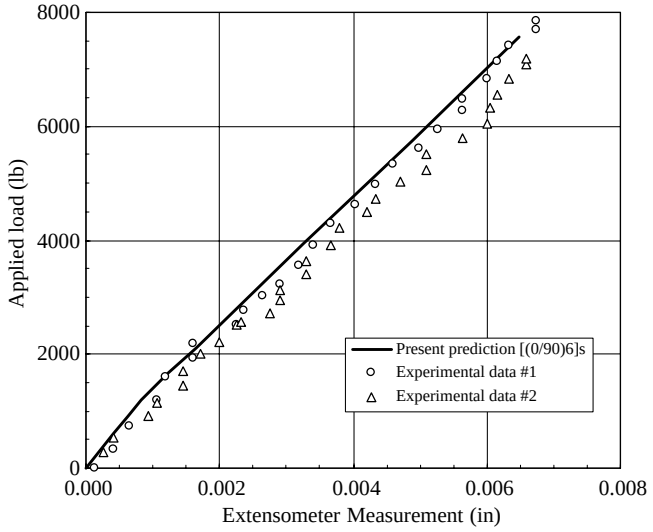

Fig. 8. Comparison of load–displacement (shortening) curves of a $[0/90]_{6}]_s$ specimen between the present prediction and experimental data (Chang and Lessard, 1991).

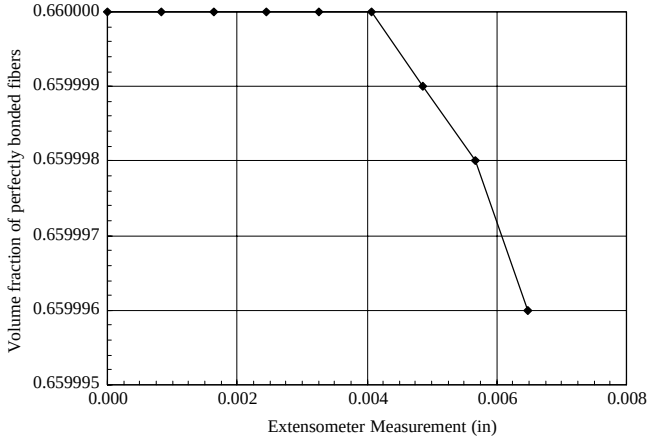

Fig. 9. The predicted evolution of volume fraction of perfectly bonded fibers versus displacement corresponding to the predicted p–u curve in Fig. 8.

both layers is one half of the plate thickness. We adopt the material properties of the laminated composite plate according to Table 1 of Chang and Lessard (1991) and Table 1.2 of Herakovich (1998) as follows: $E_0 = 4.62$ GPa, $E_1 = 238.56$ GPa; $v_0 = 0.36$, $v_1 = 0.20$; $\phi_1 = 0.66$, $\phi_2 = 0.001$. The fiber debonding and microcrack nucleation parameters involving this simulation are assumed to be $S_o = 1.65$ GPa, $M = 4.0$; $\epsilon^{th} = 0.05\%$, $c_1 = 0.4$, $c_2 = 1.8$.

We compute the applied compressive load and the relative displacement between two points located 1/2 in. (12.7 mm) above and below from the center of the hole as shown in Fig. 7(a) and compare them with the experimental data (Chang and Lessard, 1991). The predicted load–displacement (p–u) curve between the two points around the hole of the specimen is shown in Fig. 8. We also depict the experimental data (Chang and Lessard, 1991) in the figure for comparison. Figs. 9 and 10 exhibit predicted evolutions of perfectly bonded fibers and partially debonded fibers, respectively, versus displacement of the specimen corresponding to the predicted p–u curve in Fig. 8. To illustrate the nucleation of microcracks, the predicted volume fraction of microcracks is presented in Fig. 11. It is observed from Fig. 8 that the curves based on the present

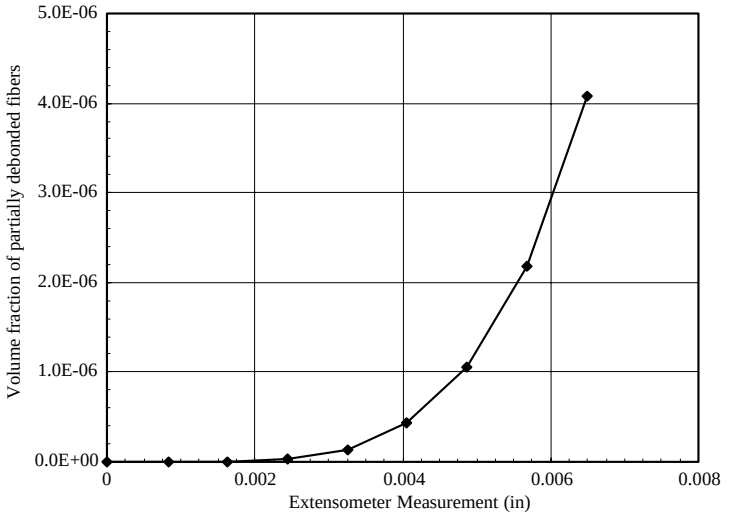

Fig. 10. The predicted evolution of volume fraction of partially debonded fibers versus displacement corresponding to the predicted p–u curve in Fig. 8.

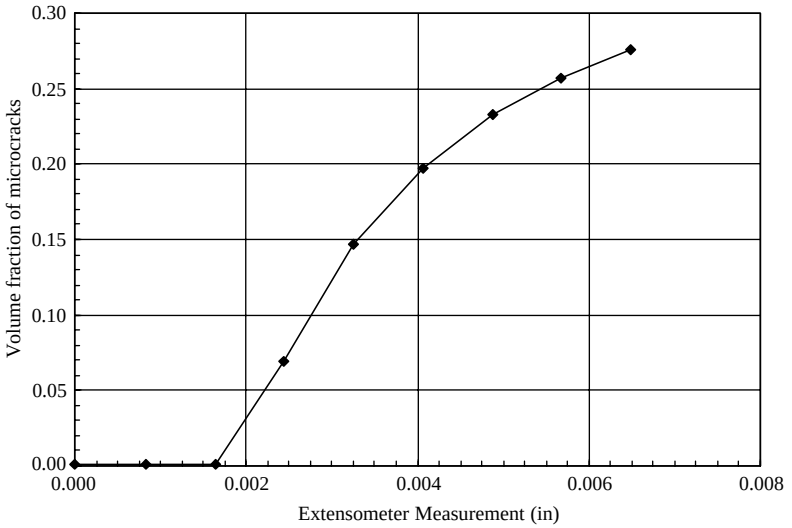

Fig. 11. The predicted evolution of volume fraction of microcracks versus displacement corresponding to the predicted p–u curve in Fig. 8.

prediction and the experiment match well throughout the entire deformation. The good agreement between the present prediction and the experiment is encouraging for possible use of the proposed computational model for predicting the elastic behavior of laminated composites.

5. Concluding remarks

A micromechanics-based constitutive model incorporating damage models was proposed to model the effective elastic behavior of unidirectional laminated composites. First, we adopted a newly developed Eshelby's tensor for an infinite circular cylindrical inclusion (Cheng and Batra, 1999) to model the unidirectional fibers and incorporated it into the micromechanical framework. The progressive loss of strength resulting from the partial fiber debonding and the nucleation of microcracks was incorporated into the constitutive model. The predicted effective stiffness of transversely isotropic composites under far field loading conditions based on the proposed constitutive model was compared with analytical solutions to validate the proposed constitutive model. Finally, the constitutive model incorporating the damage models was implemented into the finite element code ABAQUS to solve boundary value problems and to numerically characterize the elastic behavior of laminated composites. Moreover, the present predictions on the behavior of laminated composite plate containing an open hole were compared with experimental data to verify the predictive capability of the computational model.

The results indicate that the proposed computational model is capable of predicting the performance of structural components made of laminated composites. In addition, the effects of ply orientation on the response of the laminate composites are also addressed. However, the model needs to be extended to accommodate other damage mechanisms (e.g., delamination) and failure criteria to realistically characterize the damage mechanisms and failure in laminated composites. Accordingly, experimental studies to verify the model parameters and further assessment of the model will be carried out in the future.

Acknowledgments

This research was partially supported by National Computational Science Alliance under MSS020010N and utilized the IBM P690 supercomputer. The authors would also like to thank the Ministry of Science and Technology, Korea, for the financial support by a grant (No. NC 33676, R11-2002-101-02004-0) from the Smart Infra-Structure Technology Center (SISTeC), Korea.

Appendix A. Parameters $\tau_1,\ldots,\tau_6$ in Eq. (26)

These parameters take the form:

$$
\begin{aligned}
\tau_1 &= 2\mu_0 \sum_{r=1}^{3} (m_r)_1, \\
\tau_2 &= 2\mu_0 \sum_{r=1}^{3} (m_r)_2, \\
\tau_3 &= \lambda_0 \sum_{r=1}^{3} [(m_r)_1 + 4(m_r)_2 + 3(m_r)_3] + 2\mu_0 \sum_{r=1}^{3} (m_r)_3, \\
\tau_4 &= 2\mu_0 \sum_{r=1}^{3} (m_r)_4, \\
\tau_5 &= \lambda_0 \left\{ 1 + \sum_{r=1}^{3} [(m_r)_4 + 3(m_r)_5 + 2(m_r)_6] \right\} + 2\mu_0 \sum_{r=1}^{3} (m_r)_5, \\
\tau_6 &= 2\mu_0 \left[\frac{1}{2} + \sum_{r=1}^{3} (m_r)_6 \right],
\end{aligned}
\tag{46}
$$

in which $(m_r)_1,\ldots,(m_r)_6$ are the parameters of the fourth-rank tensor $\widetilde{F}_{ijkl}[(m_r)_1,\ldots,(m_r)_6]$, which is the product between $\widetilde{F}_{ijkl}[\phi_r(b_r)_1,\ldots,\phi_r(b_r)_6]$ and $\widetilde{F}_{ijkl}[(l_r)_1,\ldots,(l_r)_6]$. $\widetilde{F}_{ijkl}[(l_r)_1,\ldots,(l_r)_6]$ is the inverse of $\widetilde{F}_{ijkl}[(j_r)_1,\ldots,(j_r)_6]$ with the following parameters:

$$\begin{aligned}
(j_r)_1 &= \phi_r\big\{-(S_r)_1[(b_r)_1+4(b_r)_2+(b_r)_3+2(b_r)_6]-4(S_r)_2[(b_r)_1+2(b_r)_2+(b_r)_3]\\
&\quad -(S_r)_4[(b_r)_1+4(b_r)_2+3(b_r)_3]-2(S_r)_6(b_r)_1\big\},\\
(j_r)_2 &= \phi_r\big\{-2(S_r)_2[(b_r)_2+(b_r)_6]-2(S_r)_6(b_r)_2\big\},\\
(j_r)_3 &= \phi_r\big\{-(S_r)_3[(b_r)_1+4(b_r)_2+(b_r)_3+2(b_r)_6]-(S_r)_5[(b_r)_1+4(b_r)_2+3(b_r)_3]-2(S_r)_6(b_r)_3\big\},\\
(j_r)_4 &= \phi_r\big\{-(S_r)_1[(b_r)_4+(b_r)_5]-4(S_r)_2[(b_r)_4+(b_r)_5]-(S_r)_4[(b_r)_4+3(b_r)_5+2(b_r)_6]-2(S_r)_6(b_r)_4\big\},\\
(j_r)_5 &= \phi_r\big\{-(S_r)_3[(b_r)_4+(b_r)_5]-(S_r)_5[(b_r)_4+3(b_r)_5+2(b_r)_6]-2(S_r)_6(b_r)_5\big\},\\
(j_r)_6 &= \tfrac{1}{2}-\phi_r[2(S_r)_6(b_r)_6].
\end{aligned} \tag{47}$$

In addition, $(b_r)_1,\ldots,(b_r)_6$ are the parameters of the fourth-rank tensor $\widetilde{F}_{ijkl}[(b_r)_1,\ldots,(b_r)_6]$, which is the inverse of $\widetilde{F}_{ijkl}[(d_r)_1,\ldots,(d_r)_6]$ with the following parameters:

$$\begin{aligned}
&(d_1)_1=(S_1)_1, \qquad (d_1)_2=(S_1)_2,\\
&(d_1)_3=(S_1)_3, \qquad (d_1)_4=(S_1)_4,\\
&(d_1)_5=\frac{1}{3}\left(\frac{\kappa_0}{\kappa_1-\kappa_0}-\frac{\mu_0}{\mu_1-\mu_0}\right)+(S_1)_5,\\
&(d_1)_6=\frac{1}{2}\frac{\mu_0}{\mu_1-\mu_0}+(S_1)_6;
\end{aligned} \tag{48}$$

$$\begin{aligned}
&(d_2)_1=(S_2)_1, \qquad (d_2)_2=(S_2)_2,\\
&(d_2)_3=(S_2)_3, \qquad (d_2)_4=(S_2)_4,\\
&(d_2)_5=(S_2)_5, \qquad (d_2)_6=-\frac{1}{2}+(S_2)_6;
\end{aligned} \tag{49}$$

$$\begin{aligned}
(d_3)_1 &= 2e_1\mu_0+(S_3)_1,\\
(d_3)_2 &= 2e_2\mu_0+(S_3)_2,\\
(d_3)_3 &= 2e_3\mu_0+(S_3)_3,\\
(d_3)_4 &= e_1\lambda_0+4e_2\lambda_0+2e_4\mu_0+(S_3)_4,\\
(d_3)_5 &= e_3\lambda_0+2e_5\mu_0+2e_6\lambda_0+(S_3)_5,\\
(d_3)_6 &= 2e_6\mu_0+(S_3)_6,
\end{aligned} \tag{50}$$

where $e_1,\ldots,e_6$ in Eq. (50) are the parameters of the fourth-rank tensor $\widetilde{F}_{ijkl}[e_1,\ldots,e_6]$, which is the inverse of $\widetilde{F}_{ijkl}[f_1,\ldots,f_6]$ with the following parameters:

$$\begin{aligned}
f_1 &= \frac{9\mu_1\kappa_1}{3\kappa_1+4\mu_1}+\mu_1,\\
f_2 &= -\mu_1,\\
f_3 &= -\frac{9\mu_1\kappa_1}{3\kappa_1+4\mu_1}+\mu_1,\\
f_4 &= -\frac{9\mu_1\kappa_1}{3\kappa_1+4\mu_1}+\mu_1,\\
f_5 &= \frac{9\mu_1\kappa_1}{3\kappa_1+4\mu_1}-\mu_1-\lambda_0,\\
f_6 &= \mu_1-\mu_0.
\end{aligned} \tag{51}$$

Appendix B. Transformation matrices $\mathbf{T}_1$ in Eq. (39) and $\mathbf{T}_2$ in Eq. (40)

These matrices are given by

$$\mathbf{T}_1 = \begin{bmatrix} \cos^2\theta & \sin^2\theta & 0 & 0 & 0 & 2\cos\theta\sin\theta \\ \sin^2\theta & \cos^2\theta & 0 & 0 & 0 & -2\cos\theta\sin\theta \\ 0 & 0 & 1 & 0 & 0 & 0 \\ 0 & 0 & 0 & \cos\theta & -\sin\theta & 0 \\ 0 & 0 & 0 & \sin\theta & \cos\theta & 0 \\ -\cos\theta\sin\theta & \cos\theta\sin\theta & 0 & 0 & 0 & \cos^2\theta - \sin^2\theta \end{bmatrix}, \tag{52}$$

$$\mathbf{T}_2 = \begin{bmatrix} \cos^2\theta & \sin^2\theta & 0 & 0 & 0 & \cos\theta\sin\theta \\ \sin^2\theta & \cos^2\theta & 0 & 0 & 0 & -\cos\theta\sin\theta \\ 0 & 0 & 1 & 0 & 0 & 0 \\ 0 & 0 & 0 & \cos\theta & -\sin\theta & 0 \\ 0 & 0 & 0 & \sin\theta & \cos\theta & 0 \\ -2\cos\theta\sin\theta & 2\cos\theta\sin\theta & 0 & 0 & 0 & \cos^2\theta - \sin^2\theta \end{bmatrix}. \tag{53}$$

Appendix C. Components of $\overline{\mathbf{C}}$ in Eq. (42)

These components are

$$\begin{aligned} \overline{C}_{11} &= c^4C_{11} + 2c^2s^2C_{12} + s^4C_{22} + 4c^2s^2C_{55}, \\ \overline{C}_{22} &= s^4C_{11} + 2c^2s^2C_{12} + c^4C_{22} + 4c^2c^2C_{55}, \\ \overline{C}_{33} &= C_{22}, \\ \overline{C}_{23} &= s^2C_{12} + c^2C_{23}, \\ \overline{C}_{13} &= c^2C_{12} + s^2C_{23}, \\ \overline{C}_{12} &= c^2s^2C_{11} + (c^4 + s^4)C_{12} + c^2s^2C_{22} - 4c^2s^2C_{55}, \\ \overline{C}_{44} &= s^2C_{55} + c^2C_{44}, \\ \overline{C}_{55} &= c^2C_{55} + s^2C_{44}, \\ \overline{C}_{45} &= -csC_{44} + csC_{55}, \\ \overline{C}_{66} &= c^2s^2C_{11} + (c^2 - s^2)^2C_{55} + c^2s^2C_{22} - 2c^2s^2C_{12}, \\ \overline{C}_{16} &= c^3sC_{11} - 2cs(c^2 - s^2)C_{55} + cs(s^2 - c^2)C_{12} - cs^3C_{22}, \\ \overline{C}_{26} &= cs^3C_{11} + 2cs(c^2 - s^2)C_{55} + cs(c^2 - s^2)C_{12} - c^3sC_{22}, \\ \overline{C}_{36} &= -csC_{23} + csC_{12}, \end{aligned} \tag{54}$$

in which $c = \cos\theta$ and $s = \sin\theta$.

References

ABAQUS, 2002. ABAQUS Example Problems Manual, Version 6.3, Hibbitt, Karlsson & Sorensen, Inc., Pawtucket, RI.

Chajes, M.J., Januszka, T.F., 1995. Shear strengthening of reinforced concrete beams using externally applied composite fabrics. ACI Struct. J. 92, 295–303.

Chang, F.K., Lessard, L., 1991. Damage tolerance of laminated composites containing an open hole and subjected to compressive loadings: Part I—Analysis. J. Compos. Mater. 25, 2–43.

Cheng, Z.Q., Batra, R.C., 1999. Exact Eshelby tensor for a dynamic circular cylindrical inclusion. J. Appl. Mech. 66, 563–565.

Eshelby, J.D., 1957. The determination of the elastic field of an ellipsoidal inclusion, and related problems. Proc. R Soc. Lond. A 241, 376–396.

Eshelby, J.D., 1961. Elastic inclusions and inhomogeneities. In: Sneddon, I.N., Hill, R. (Eds.), Progress in Solid Mechanics. North-Holland Publisher Co, Amsterdam.

Herakovich, C.T., 1998. Mechanics of Fibrous Composites. John Wiley & Sons, New York.

Hill, R., 1964. Theory of mechanical properties of fiber-strengthened materials: I. Elastic behavior. J. Mech. Phys. Solids 12, 199–212.

Ju, J.W., Chen, T.M., 1994. Micromechanics and effective moduli of elastic composites containing randomly dispersed ellipsoidal inhomogeneities. Acta Mechanica 103, 103–121.

Ju, J.W., Lee, H.K., 2000. A micromechancial damage model for effective elastoplastic behavior of ductile matrix composites considering evolutionary complete particle debonding. Comput. Meth. Appl. Mech. Eng. 183, 201–222.

Ju, J.W., Lee, H.K., 2001. Micromechanical damage model for effective elastoplastic behavior of partially debonded ductile matrix composites. Int. J. Solids Struct. 38, 6307–6332.

Karihaloo, B.L., Fu, D., 1989. A damage-based constitutive law for plain concrete in tension. Eur. J. Mech., A-Solids 8, 373–384.

Karihaloo, B.L., Fu, D., 1990. Orthotropic damage model for plain concrete in tension. ACI Mater. J. 87, 62–67.

Lee, H.K., Liang, Z., 2004. Computational modeling of the response and damage behavior of fiber reinforced cellular concrete. Comput. Struct. 82, 581–592.

Lee, H.K., Shin, D.K., 2004. A computational investigation of crack evolution and interactions of microcracks and particles in particle-reinforced brittle composites. Compos. Struct. 64, 419–431.

Lee, H.K., Simunovic, S., 2001. A damage constitutive model of progressive debonding in aligned discontinuous fiber composites. Int. J. Solids Struct. 8, 875–895.

Mikata, Y., Nemat-Nasser, S., 1990. Elastic field due to a dynamically transforming spherical inclusion. J. Appl. Mech. 57, 845–849.

Mikata, Y., Nemat-Nasser, S., 1991. Interaction of a harmonic wave within a dynamically transforming inhomogeneity. Journal of Applied Physics 70, 845–849.

Mura, T., 1982. Micromechanics of Defects in Solids. Martinus Nijhoff Publishers, Dordrecht, Netherlands.

Sun, L.Z., 1998. Micromechanics and overall elastoplasticity of discontinuously reinforced metal matrix composites. Ph.D. Dissertation, University of California, Los Angeles.

Tungikar, V.B., Basu, S.K., Rathod, G.D., Kajale, S.R., 2004. Finite element modelling of transient thermal stresses in layered composites. J. Inst. Eng. (India), pt PR 83, 82–84.

Zhao, Y.H., Weng, G.J., 1996. Plasticity of a two-phase composite with partially debonded inclusion. Int. J. Plastic. 12, 781–804.

Zhao, Y.H., Weng, G.J., 1997. Transversely isotropic moduli of two partially debonded composites. Int. J. Solids Struct. 34, 493–507.